ADVANCED FUNCTIONAL MATERIALS
www.afm-journal.de

Advanced Aerodynamics-Driven Energy Harvesting Leveraging Galloping-Flutter Synergy

Liwei Dong, Guobiao Hu, Qian Tang, Chaoyang Zhao, Fan Yang, and Yaowen Yang**

Flow-induced vibrations (FIVs) serve as the fundamental principle of non-rotary wind energy harvesting. However, nanogenerators relying on a single FIV effect remain constrained by insufficient breeze energy conversion efficiency. In this paper, we propose a novel galloping-flutter coupled nanogenerator (GFNG) that leverages the synergistic interaction between these two aerodynamic phenomena, to achieve high performance across broad wind speed bandwidth. A galloping-flutter coupled mechanism (GFM) is implemented using a multifunctional flexible beam that integrates a galloping piezoelectric energy harvester (GPEH) and a fluttering triboelectric nanogenerator (FTENG). Through meticulous optimization, it significantly enhances the average electrical output of the FTENG by up to six times at low wind speeds below 6 m s^{-1}, by intensifying the triboelectric contact behavior through galloping-induced beam oscillations. The GFNG demonstrates a maximum average power of 6.3 mW across wind speeds from 1.4 to 10 m s^{-1}, along with a remarkable power density of 7.1 W m^{-2} of the enhanced FTENG at 10 m s^{-1}, enabling the lighting of 508 LEDs and stable power supply for wireless sensor nodes (WSNs). This study offers new insights into designing high-performance aerodynamics-driven nanogenerators by harnessing multiple FIV synergistic effects, broadening the potential for intelligent wind energy applications.

1. Introduction

Wind is widely-distributed and readily available in the natural environment. With the rapid advancement of energy harvesting technology, wind energy, as a high-entropy resource, has garnered sustained attention from researchers since the 19th century. Consequently, wind energy harvesters (WEHs) utilizing electromagnetic, piezoelectric, and triboelectric mechanisms have been developed in different sizes and power capacities to serve diverse applications.[1–4] In recent years, there has been a concerted effort to enhance the performance of small-scale wind energy harvesting. Wind energy can be captured and utilized to power wireless sensor nodes (WSNs), enabling battery-free operation and energy self-sufficiency. This advancement holds substantial potential to accelerate the proliferation of the Internet of Things (IoTs) in both urban and outdoor environments.

WEHs can be categorized into rotary and flow-induced vibration (FIV) types based on their implementation mechanisms.[5,6] Traditional rotary wind turbines harness wind energy using wind cups or windmills,[7] altering the rotary mechanical energy into electricity through electromagnetic induction principle. Since the triboelectric nanogenerator (TENG) was first proposed in 2012,[8] the development of rotary WEHs has sparked a new wave.[9] TENGs exhibit superiority in low-frequency mechanical energy harvesting,[10] and their diverse working modes enable rotary WEHs to be more miniaturized and lightweight. To improve the wind energy harvesting performance of TENGs, strategies such as material improvement,[11–13]

L. Dong, C. Zhao, Y. Yang
School of Civil and Environmental Engineering
Nanyang Technological University
50 Nanyang Avenue, Singapore 639798, Singapore
E-mail: cywyang@ntu.edu.sg
L. Dong
College of Transportation
Tongji University
Shanghai 201804, China
G. Hu
Internet of Things Thrust
The Hong Kong University of Science and Technology (Guangzhou)
Nansha, Guangzhou, Guangdong 511400, China
Q. Tang
Chongqing Key Laboratory of Green Energy Materials Technology and System
Chongqing University of Technology
Chongqing 400054, China
F. Yang
Department of Orthopaedics
Shanghai Key Laboratory for Prevention and Treatment of Bone and Joint Diseases
Shanghai Institute of Traumatology and Orthopaedics
Ruijin Hospital
Shanghai Jiao Tong University School of Medicine
Shanghai 200025, China
E-mail: yf12498@sjtu.edu.cn
F. Yang
Research Institute of Frontier Science
Southwest Jiaotong University
Chengdu, Sichuan 610031, China

The ORCID identification number(s) for the author(s) of this article can be found under https://doi.org/10.1002/adfm.202414324

DOI: 10.1002/adfm.202414324

structural optimization,[14–16] and interface circuit design[17,18] have been widely explored. Moreover, the integration of TENGs with electromagnetic generators (EMGs) has emerged as a key research trend aimed at improving space utilization and power density.[19–22] In this setup, the TENG provides a higher output voltage, while the EMG delivers a larger current, creating a complementary power generation system.[23–25] Zheng et al.[26] proposed a compact triboelectric-electromagnetic nanogenerator for self-powered applications in a ventilation system. The blades and air inlet covers were optimized to enhance the utilization of wind energy, achieving a peak current of 0.05 A at a wind speed of 6.5 m s^{-1}. Zhu et al.[27] developed a TENG-EMG hybrid nanogenerator to power a wireless weather station. Lift-drag hybrid blades were utilized to weaken the wind resistance, resulting in an 11% performance improvement and a peak efficiency of 9.1% at 4 m s^{-1}. However, challenges persist in achieving low startup wind speeds (typically 3–4 m s^{-1}) and improving performance at low wind speeds. These limitations are primarily due to the static friction and inertial forces associated with rotors.

FIV-based WEHs refer to harvesters utilizing aerodynamic phenomena including vortex-induced vibration (VIV), flutter, galloping, and wake galloping.[28,29] Early designs of FIV-based WEHs predominantly employed piezoelectric mechanisms,[30–41] but the introduction of TENGs has led to new forms of FIV-based WEH devices.[42–46] Owing to the flexibility of numerous triboelectric materials, fluttering TENGs (FTENGs) are becoming a new hotspot in wind energy harvesting.[47] They can be miniaturized into flag-like structures, either interwoven[48] or glued[49] using two types of triboelectric materials with opposite polarities. Performance can be enhanced by positioning bluff bodies at the front[50] or using the flapping behavior between two flags.[51] To maximize wind energy harvesting efficiency, the fluttering flag can be designed to achieve optimal contact by flapping against one or both side baffles.[52–54] To further improve the contact behavior, Zhang et al.[55] developed a flexible flagpole that oscillates between two baffles to intensify the flag flutter. However, the flexible flagpole operates effectively only at high wind speeds, and thus does not significantly boost the low-speed wind energy conversion efficiency of FTENGs. While using flexible materials for FIV-based WEHs allows for breeze energy harvesting, the conversion efficiency remains suboptimal.

The hybridization of piezoelectricity and triboelectricity has emerged as another promising approach for efficiency improvement. Advanced and compact designs have been developed. For instance, Qin et al.[56] built an intelligent squirrel cage with a highly integrated piezoelectric-triboelectric design for aero-engines to enable simultaneous energy harvesting and self-sensing applications. The device achieved a maximum power output of 100 μW at a rotational frequency of 15 Hz. Zheng et al.[57] tightly combined piezoelectric and triboelectric components to obtain an all-in-one mechanical energy harvester featuring the structure of a three-phase asynchronous generator. The compact design delivered a 500 V voltage and 1.1 mA current under a vibration excitation at 4 Hz. Based on the above review, future performance improvements for FIV-based WEHs are anticipated from the following two perspectives: (1) integrating piezoelectric and triboelectric mechanisms, two main mechanisms of FIV-based WEHs, to improve space utilization efficiency; (2) and synergistically leveraging multiple forms of FIVs to achieve enhanced wind energy conversion efficiency.

Thus, this paper proposes a novel galloping-flutter coupled nanogenerator (GFNG) leveraging the synergistic effect of galloping and flutter for enhanced wind energy harvesting. The galloping-flutter coupled mechanism (GFM) integrates a galloping piezoelectric energy harvester (GPEH) into an FTENG through a multifunctional flexible beam, with minimal increase in device volume. The GPEH delivers outstanding continuous power output, while the FTENG offers superior instantaneous power output, achieving complementary operational properties. Additionally, the GFM improves the contact behavior, significantly boosting the FTENG's performance at wind speeds below 6 m s^{-1} through galloping-induced beam oscillations. The flexible beam, as the critical component of the GFM, is meticulously designed based on a distributed aero-electro-mechanical model of the GPEH that accounts for local stiffness variation, followed by experimental optimization for structural parameters including bluff body height, baffle distance, flag length and triboelectric material layer. The GFNG achieves an average power output of 70 μW-6.3 mW across wind speeds from 1.4 to 10 m s^{-1}, along with a power density of 7.1 W/m^2 of the FTENG at 10 m s^{-1}. Through application demonstrations, including lighting LEDs and powering WSNs, the GFNG demonstrates its potential for diverse self-powered applications, highlighting its innovative design that fully capitalizes on the advantages of galloping and flutter phenomena.

2. Results and Discussion

2.1. Configuration and Principle of GFNG

Our study aims to design a high-performance nanogenerator capable of ensuring the continuous operation of multiple sensors and supporting various self-powered applications. As illustrated in **Figure 1a**, the proposed nanogenerator can be deployed in windy environments such as railways and coastal areas to facilitate battery-free environmental monitoring and self-powered alarm systems. Additionally, it can be adapted for specific scenarios, such as ventilation systems, where it can function as an independent module to detect smoke and monitor air quality when integrated with gas sensors.

As TENG technology advances, FTENGs have emerged as one of the most effective non-rotary wind energy harvesting approaches. However, the fluttering contact between the conductive membrane and the triboelectric materials inside baffles is usually insufficient, leaving a large portion of potential contact surfaces underutilized. A flexible flagpole was recently proposed to utilize its wind-induced oscillation to enlarge the contact surface and improve the energy harvesting capacity of FTENGs.[55] Nevertheless, triggering flagpole oscillation requires a wind speed of at least 5.5 m s^{-1}, limiting performance improvements in most natural wind conditions. To address this limitation, as depicted in Figure 1b, we propose a novel GFNG that incorporates a GPEH and an FTENG. These two components are connected via a flexible beam, with the FTENG's flexible flag attached to the beam. To trigger beam galloping at low-speed winds and improve the contact behavior in the FTENG, a bluff body is configured at the top of the flexible beam. This configuration naturally

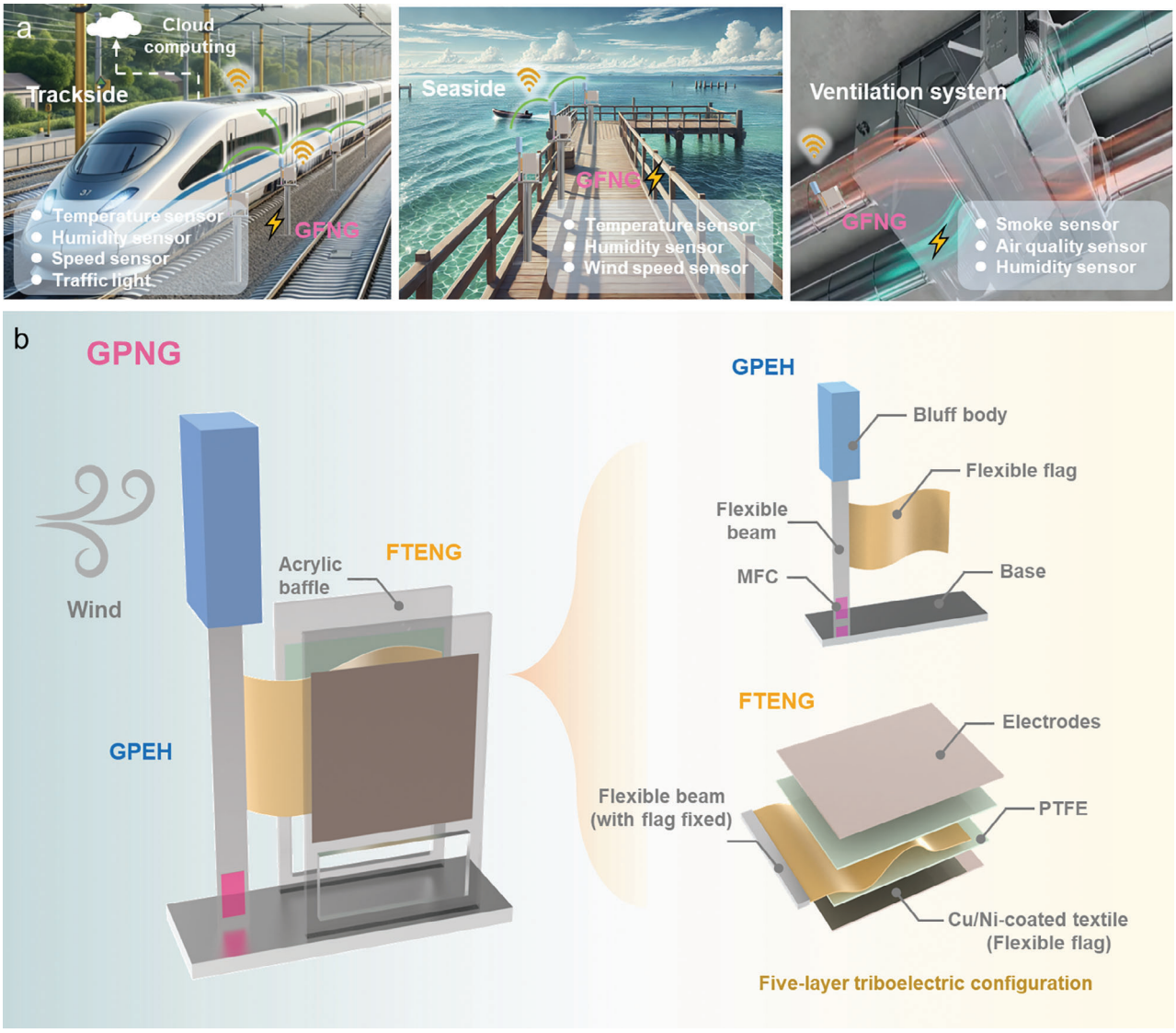

Figure 1. Application scenarios and configuration of GFNG: a) illustration of GFNG applied in trackside, seaside, and ventilation systems; b) configuration of GFNG.

integrates a GPEH by attaching a Macro Fiber Composite (MFC) near the fixed end of the flexible beam, converting galloping-induced strain into electricity. The introduction of the GPEH can significantly boost the overall performance of the GFNG with minimal increase in device volume. The FTENG adopts a five-layer configuration, wherein the fluttering part is made of Cu/Ni-coated textile and the stationary parts on both sides employ PTFE membranes and copper electrodes. The microstructures of conductive textile and PTFE membrane under scanning electron microscope (SEM) are supplemented in Figure S1 (Supporting Information).

The galloping phenomenon involves large-amplitude oscillations that occur on an elastically mounted bluff body when the wind speed exceeds the cut-in wind speed. The dynamics of the galloping structure can be governed as:

$$M_e\ddot{\omega}(L,t) + D_e\dot{\omega}(L,t) + K_e\omega(L,t) = F_y(t) \quad (1)$$

where M_e, D_e, and K_e refer to the mass of the bluff body, the system damping coefficient, and the system stiffness; F_y denotes the galloping force. $\omega(L, t)$ represents the bluff body displacement.

Figure 2a presents the working principle and charge variation of the GPEH during a single period of galloping motion of the flexible beam, and the electromechanical coupling relationship can be expressed as:

$$C_p\dot{V}_p(t) + I_p(t) - \theta\int_{L_1}^{L_2}\frac{\partial^3\omega(x,t)}{\partial x^2\partial t}dx = 0 \quad (2)$$

where C_p refers to the internal capacitance of the MFC; V_p and I_p are the voltage and current across the circuit; θ represents the electromechanical coupling coefficient; L_1 and L_2 are the positions of both ends of the MFC on the beam; $\omega(x, t)$ refers to the beam deflection relative to position x and time t.

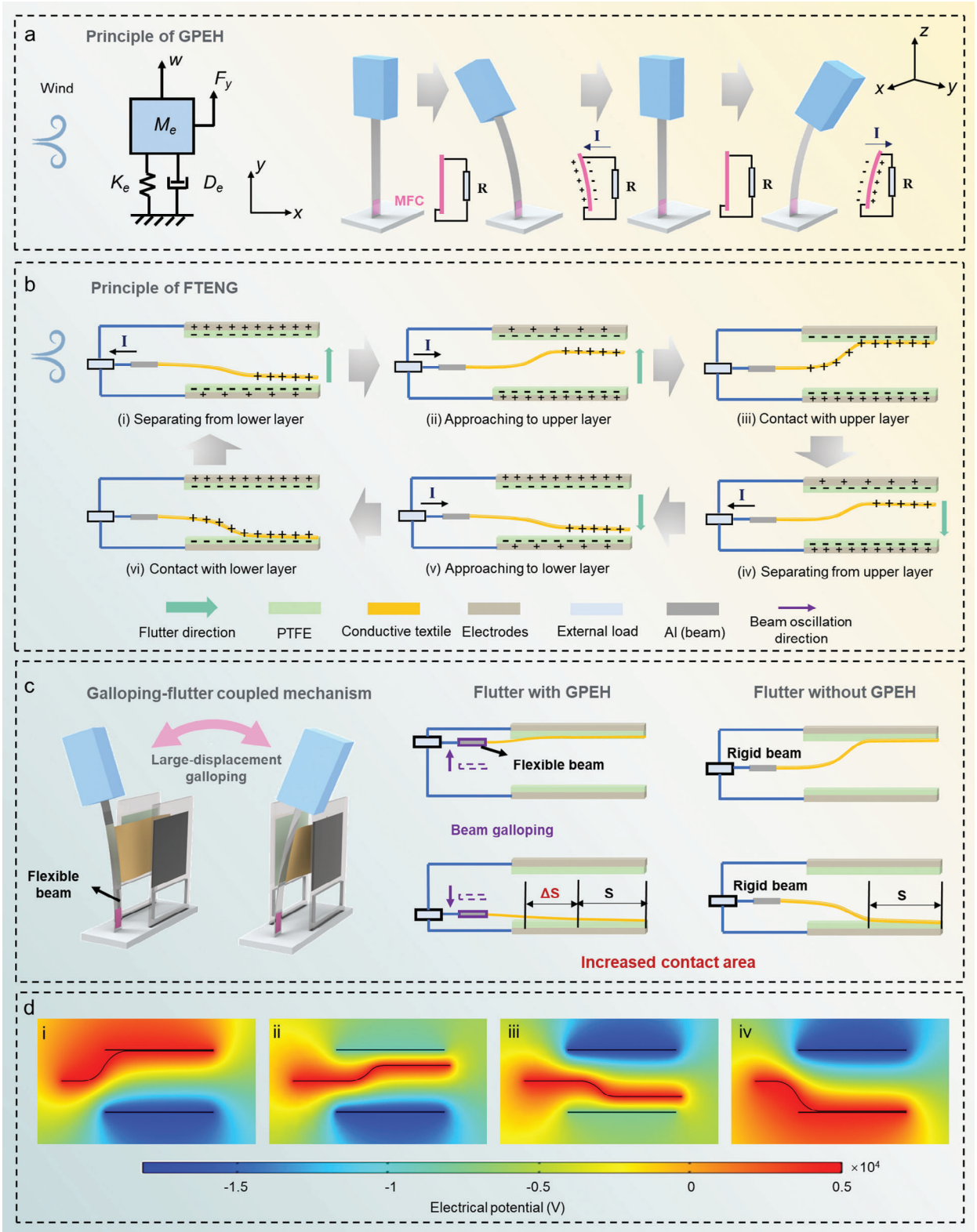

Figure 2. Working principle of GFNG: a) working principle of GPEH and b) FTENG; c) principle of the GFM improving the contact behavior of FTENG; d) electrical potential simulation of FTENG under an ideal contact situation.

When the wind flows across the FTENG, the conductive textile flutters and contacts with the PTFE membranes inside the baffles, resulting in cyclic charge variations, as illustrated in Figure 2b. A complete depiction of the charge variation from the initial state is supplemented in Figure S2 (Supporting Information). The voltage of the FTENG with a five-layer configuration can be governed as

$$V_t = \frac{\delta x(t)}{\varepsilon_0} - \frac{Q}{S\varepsilon_0}\left(\frac{d_1}{\varepsilon_1} + x(t)\right) \tag{3}$$

where δ refers to the surface charge density; ϵ_0 indicates the permittivity of vacuum; Q indicates the transferred charge; S denotes the contact area; d_1 and ϵ_1 represent the dielectric layer thickness and its relative dielectric constant; $x(t)$ denotes the distance between two triboelectric layers.

The GFM is typically implemented using a flexible beam with a relatively low stiffness, allowing sufficient oscillation to increase the contact surface, thereby enhancing the energy harvesting capacity of the FTENG. As shown in Figure 2c, when the GPEH undergoes periodic galloping, the beam oscillates, leading to periodic displacement at the fixed end of the flag. The absolute displacement of the flag is the sum of the beam's lateral displacement and the flag's fluttering displacement. Consequently, a larger contact area S with the triboelectric layers inside the two sides of the baffles can be achieved, generating a higher voltage according to Equation (3). This indicates that in the GFNG, the GPEH and FTENG are not merely assembled but are synergistically enhanced through galloping-flutter coupling, facilitating additional performance improvements. Figure 2d simulates the electrical potential of the FTENG under an ideal contact situation with commercial software COMSOL. The maximum potential difference can exceed 2000 V, highlighting the exceptional power generation capacity of the FTENG.

2.2. Superiority of Galloping-Flutter Coupled Mechanism

To demonstrate the advantages of the GFM, the performance of the FTENG with/without GFM (see **Figure 3a**) is compared. The wind tunnel test setup for the GFNG is illustrated in Figure S3 (Supporting Information). As depicted in Figure 3b,c, the GPEH takes a few seconds to initiate galloping, during which the galloping displacement and GPEH voltage gradually increase to a steady state. Simultaneously, the voltage of the FTENG increases with the onset of galloping, and the final peak voltage is tripled compared to a conventional FTENG without GFM. To evaluate the improvement in continuous power generation, the RMS voltage of the FTENG with/without GFM at different wind speeds is compared in Figure 3d. The RMS voltage improvement ratio increases from 1.4 to 2.5 as the wind speed rises from 2.7 to 3.7 m s^{-1}, due to the increased galloping displacement. However, this improvement ratio declines continuously at higher wind speeds. This can be attributed to three factors: (1) the flutter-induced contact of the FTENG is more effective at high wind speeds; (2) the flutter frequency increases rapidly with wind speed and can reach up to 50 Hz (see Figure S4, Supporting Information), whereas galloping is a low-frequency vibration whose frequency remains relatively constant, thus diluting the RMS performance improvement; (3) the increase in peak-to-peak voltage induced by the GPEH also generally declines with wind speed (see Figure S5, Supporting Information). Correspondingly, in Figure 3e, the improvement ratio of average power with GFM can be up to 6 times at wind speeds below 6 m s^{-1}, promising better performance under natural wind conditions. On the other hand, as illustrated in Figure S6 (Supporting Information), the FTENG's flutter indicates little effect on large-amplitude galloping and the output voltage of the GPEH. Due to the extra performance improvement provided by the GFM, the integrated GFNG design achieves an enhanced synergistic effect.

In Figure 3a, we also propose an alternative GFNG design where the GPEH is configured with a flag-type FTENG (which can be realized by weaving triboelectric materials) attached behind the beam without two sides of baffles. As shown in Figure 3f,g, this configuration results in suppressed galloping and a significant reduction in the GPEH voltage. This suppression is primarily attributed to the high-frequency excitation at specific acceleration and frequency, which inhibits low-frequency galloping. Similar phenomena have been widely documented and explained in relevant literature.[58] Another possible reason is that flutter might affect the flow field around the bluff body, interfering with the normal triggering of galloping. Thus, the configuration without baffles is not applicable for wind energy harvesting. The time-domain voltages of the GPEH and FTENG for the final configuration are supplemented in Figure S7 (Supporting Information).

2.3. Flexible Beam Design with Aero-Electro-Mechanical Model

The flexible beam in the GPNG plays a crucial role in both the electrical output of the GPEH and the enhancement effect for the FTENG, making its parameter selection essential. To address this, we introduce a distributed aero-electro-mechanical coupling model for the GPEH, which accounts for the local stiffness variation of the composite beam.

The model is established based on the Euler-Bernoulli beam theory, incorporating the aerodynamic galloping force as well as piezoelectric and electromechanical coupling effects (see **Figure 4a**). Thus, the motion of the GPEH is governed as

$$\begin{aligned} &EI\frac{\partial^4\omega(x,t)}{\partial x^4} + C_a\frac{\partial\omega(x,t)}{\partial t} + C_sI\frac{\partial^5\omega(x,t)}{\partial x^4\partial t} + m\frac{\partial^2\omega(x,t)}{\partial t^2} \\ &+\theta V_p(t)\left[\frac{d\delta(x-L_2)}{dx} - \frac{d\delta(x-L_1)}{dx}\right] = F_y(t)\delta(x-L) \end{aligned} \tag{4}$$

$$\theta = -E_p d_{31} W_p h_{pc} \tag{5}$$

where EI indicates the composite beam's bending stiffness; C_a and C_s represent the strain and viscous air damping coefficients; m refers to the mass per unit length of the composite beam; $\delta(x)$ indicates to the Dirac delta function; E_p and d_{31} represent the Young's modulus and the piezoelectric constant of the MFC; W_p and h_{pc} denote the MFC width and the distance from the MFC center to the neutral axis, respectively.

Given that the MFC is configured at the beam's fixed end and its thickness cannot be ignored, accurate modeling must account for the impact of its stiffness on the beam. For the case where the piezoelectric sheet does not fully cover the beam, the beam

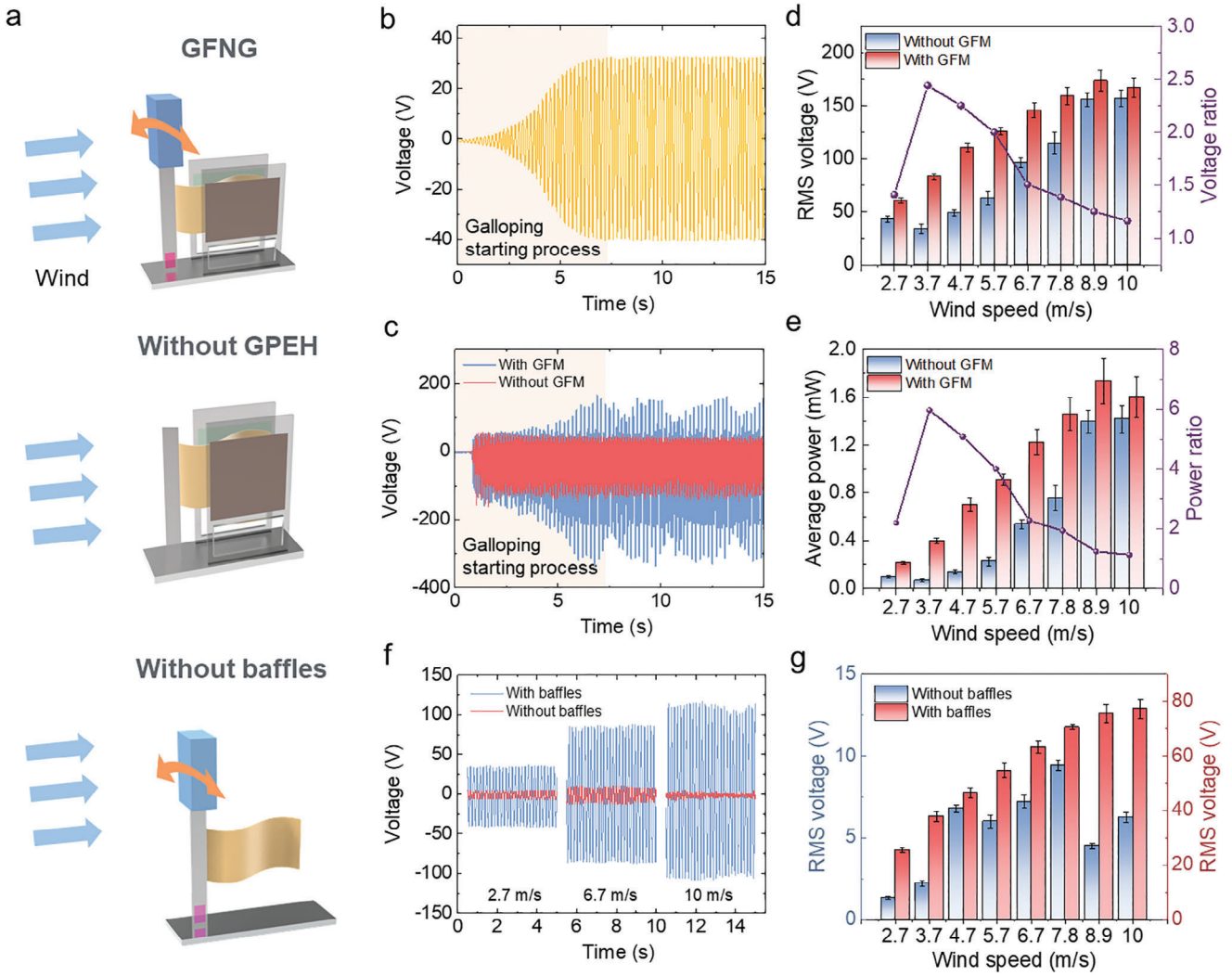

Figure 3. Performance enhancement with GFM: a) illustration of GFNG and its configurations without GPEH and baffles; b) open-circuit voltage of GPEH and c) FTENG with/without GFM at 2.7 m s^{-1}; d) RMS voltage and e) average power improvement with GFM; f) open-circuit voltage of GPEH (flag equipped) with/without baffles; g) comparison of open-circuit voltage of GPEH (flag equipped) with/without baffles versus wind speed.

should be divided into three sections for separate consideration, as illustrated in Figure 4b. The width of a bluff body is usually one to two orders of magnitude greater than the thickness of a beam, resulting in a much larger bending stiffness. Therefore, in theoretical modeling, the bluff body is treated as a rigid body and only its mass is considered. Correspondingly, the bending stiffness EI and mass m in the three sections can be written as:

$$EI = \begin{cases} E_s W_s T_s^3/12 & 0 \le x < L_1 \\ E_s W_s \left(T_b^3 - T_a^3\right)/3 + E_p W_p \left(T_c^3 - T_b^3\right)/3 & L_1 \le x < L_2 \\ E_s W_s T_s^3/12 & L_2 \le x < L \end{cases} \quad (6)$$

$$m = \begin{cases} \rho_s T_s W_s & 0 \le x < L_1 \\ \rho_s T_s W_s + \rho_p T_p W_p & L_1 \le x < L_2 \\ \rho_s T_s W_s & L_2 \le x < L \end{cases} \quad (7)$$

where E_s denotes the Young's modulus of the aluminum substrate; W_s and T_s denote the width and thickness of the substrate beam; T_p represents the MFC's thickness; ρ_s and ρ_p refer to the densities of the substrate beam and MFC; T_a, T_b, and T_c refer to the positions of the bottom of the substrate beam, the bottom the MFC, and the top of the MFC to the to the neutral axis, respectively; the aforementioned h_{pc} equals to $(T_b+T_c)/2$.

The lateral galloping force can be expressed as:

$$F_y(t) = \frac{1}{2}\rho H_{bf} L_{bf} U^2 \sum_{i=1}^{3} A_i a^i, a = \frac{\dot{\omega}(L,t)}{U} + \omega'(L,t) \quad (8)$$

where ρ indicates the air density; H_{bf} and L_{bf} denote the bluff body height and length; U refers to the wind speed; A_1 and A_3 are empirical values and can be determined based on static wind tunnel tests. They are usually related to bluff body cross-sections.

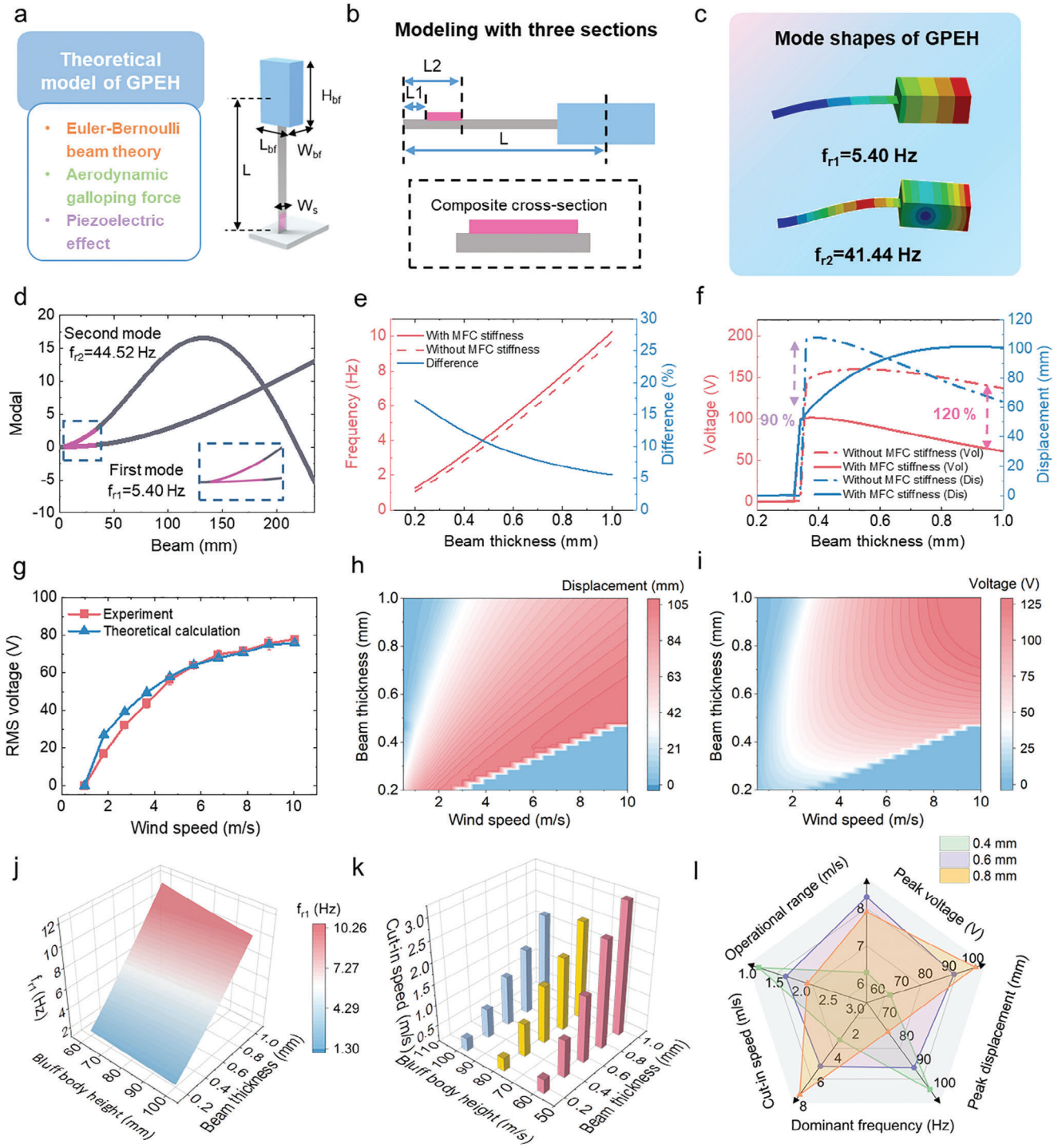

Figure 4. Theoretical analysis for flexible beam design: a) distributed aerodynamic model for GPEH; b) accurate modeling with three sections considering MFC stiffness; c) first two mode shapes of GPEH obtained by finite element simulation and d) theoretical calculation; e) comparison of first natural frequency, f) peak voltage and tip displacement calculated by theoretical model with/without considering MFC stiffness; g) validation of the theoretical model with experimental results (the beam thickness is 0.6 mm and the bluff body height is 100 mm); h) tip displacement and i) peak voltage of GPEH versus beam thickness and wind speed; j) natural frequency and k) cut-in wind speed of GPEH versus beam thickness and bluff body height; l) comprehensive comparison of three beam thickness schemes (peak displacement and voltage is the performance of GPEH at 6 m s^{-1}).

The beam deflection is usually expressed as in the modal coordinate

$$\omega_b(x,t) = \sum_{r=1}^{\infty} \varphi_r(x)\eta_r(t) \tag{9}$$

where $\varphi_r(x)$ and $\eta_r(t)$ represent the mass-normalized mode shapes of the rth modal and modal coordinate. The solving process of mode shapes can be referred to Note S1 (Supporting Information).

Thus, Equation (4) can be rewritten in the modal coordinate

$$\ddot{\eta}_r(t) + 2\zeta_r\omega_r\dot{\eta}_r(t) + \omega_r^2\eta_r(t) + \chi V(t) = f_y(t) \tag{10}$$

where ζ_r is the modal damping ratio. ω_r and f_y denote the undamped modal frequency and the galloping force in the modal coordinate, and they are given as:

$$\chi = \theta \int_{L_1}^{L_2} \varphi''_r(x)dx = \theta\left[\varphi'(L_2) - \varphi'(L_1)\right] \tag{11}$$

$$f_y(t) = \varphi_r(L) \times \frac{1}{2}\rho H_{bf} L_{bf} U^2 \sum_{i=1}^{3} A_i \left[\frac{\sum_{r=1}^{\infty}\varphi_r(L)\dot{\eta}_r(t)}{U} + \sum_{r=1}^{\infty}\varphi'_r(L)\eta_r(t)\right]^i \tag{12}$$

The Equation (2) can be rewritten in the modal coordinate

$$I_p(t) + C_p V_p(t) + \sum_{r=1}^{\infty}\chi\dot{\eta}_r(t) = 0 \tag{13}$$

Given the importance of accurately modeling stiffness variation along the beam length, we first validate the necessity of incorporating this factor. The parameters used for theoretical calculation are listed in Note S2 (Supporting Information). The mode shapes of the GPEH, accounting for MFC stiffness, are obtained through finite element simulations using the commercial software ANSYS (see Figure 4c), and supplementary simulations without MFC stiffness are provided in Figure S8a (Supporting Information), demonstrating significant differences in the results. The first two mode shapes of the GPEH calculated using the theoretical model are illustrated in Figure 4d, and exhibit strong agreement with finite element simulation results, especially for the first mode (see Figure S8b, Supporting Information). Subsequently, the natural frequency with/without MFC stiffness, as a function of beam thickness, is investigated based on the theoretical model. As depicted in Figure 4e, the influence of the MFC stiffness is more pronounced for thinner substrate beams, with a maximum difference of 17% observed at a beam thickness of 0.2 mm. Differences are also evident in the displacement and voltage output, as illustrated in Figure 4f, with maximum differences of 90% in displacement and 120% in voltage at beam thicknesses of 0.35 and 1 mm, respectively. These findings underscore the necessity of incorporating MFC stiffness in the modeling process. Finally, the distributed aerodynamic model is validated through experimental tests, as presented in Figure 4g. The strong agreement between the experimental results and theoretical analysis demonstrates the prediction accuracy of the theoretical model.

The dynamic behavior and electrical output of a GPEH heavily rely on the parameters of the beam and bluff body. According to Equation (6), the variation in beam thickness has a significant impact on the bending stiffness, consequently affecting the performance of the GPEH. Thus, the beam length and width are initially set as 235 and 20 mm, respectively, based on the expected size of the harvester. The beam thickness is then carefully optimized using the theoretical model. If the performance of the designed harvester does not meet expectations, the beam length and width can be easily re-adjusted. Similarly, according to Equation (8), the galloping force is closely related to the geometric dimensions of the bluff body. However, in the theoretical design process, the width and length of the bluff body cannot be used as variables, otherwise, the coefficients A_1 and A_3 will change correspondingly given that they are related to bluff body cross-sections.[59] Thus, the length and width of the bluff body are first pre-determined as 50 and 30 mm (A_1 and A_3 obtained from static wind tunnel tests correspondingly) based on the expected size of the harvester and our experience, with the bluff body height designed using the theoretical model. Figure 4h illustrates the tip displacement of the GPEH versus beam thickness. For a GPEH designed for a maximum operational wind speed of 10 m s^{-1}, a beam thickness of 0.5–0.6 mm is optimal for generating sufficient displacements to enhance the contact behavior of the FTENG, while yielding a considerable voltage output (see Figure 4i). A thinner beam results in greater flexibility but fails to generate the restoring force required for galloping at higher wind speeds, thus narrowing the operational bandwidth. In contrast, a thicker beam increases rigidity, leading to smaller oscillation displacement. Figure S9 (Supporting Information) shows that a larger bluff body increases both tip displacement and electrical output. However, the increase in voltage output is not significant at high wind speeds. As shown in Figure 4j, the dominant frequency of the GPEH is investigated with respect to beam thickness and bluff body height. Since galloping is a low-frequency vibration relative to high-frequency flutter (see Figure S4, Supporting Information), a higher dominant frequency is expected to enable the peak voltage components in the FTENG enhanced by galloping denser, improving the average power output. A larger bluff body and thicker beam lower the cut-in wind speed of the GPEH (see Figure 4k), benefiting the operation of both GPEH and FTENG at low wind speeds. Therefore, selecting optimal parameters requires careful consideration of multiple performance indicators.

Based on the above analysis, the GPEH's performance is observed to be more sensitive to variations in beam thickness than in bluff body height. Consequently, the bluff body height is determined as 100 mm, and three schemes (beam thickness:0.4 mm/0.6 mm/0.8 mm) are comprehensively compared in terms of operational wind speed range, output voltage, tip displacement and dominant frequency, cut-in wind speed (see Figure 4l). The time-domain displacement and voltage curves of the three schemes calculated using the theoretical model are supplemented in Figure S10 (Supporting Information). The first three indicators relate to the GPEH's performance, while the latter two pertain to its enhancement effect on the FTENG. A thinner beam of 0.4 mm results in better output voltage, greater tip displacement, and lower cut-in wind speed but a narrower operational wind speed range and lower dominant frequency, whereas a thicker beam of 0.8 mm offers the opposite results. All indicators with a thickness of 0.6 mm fall between those of the two

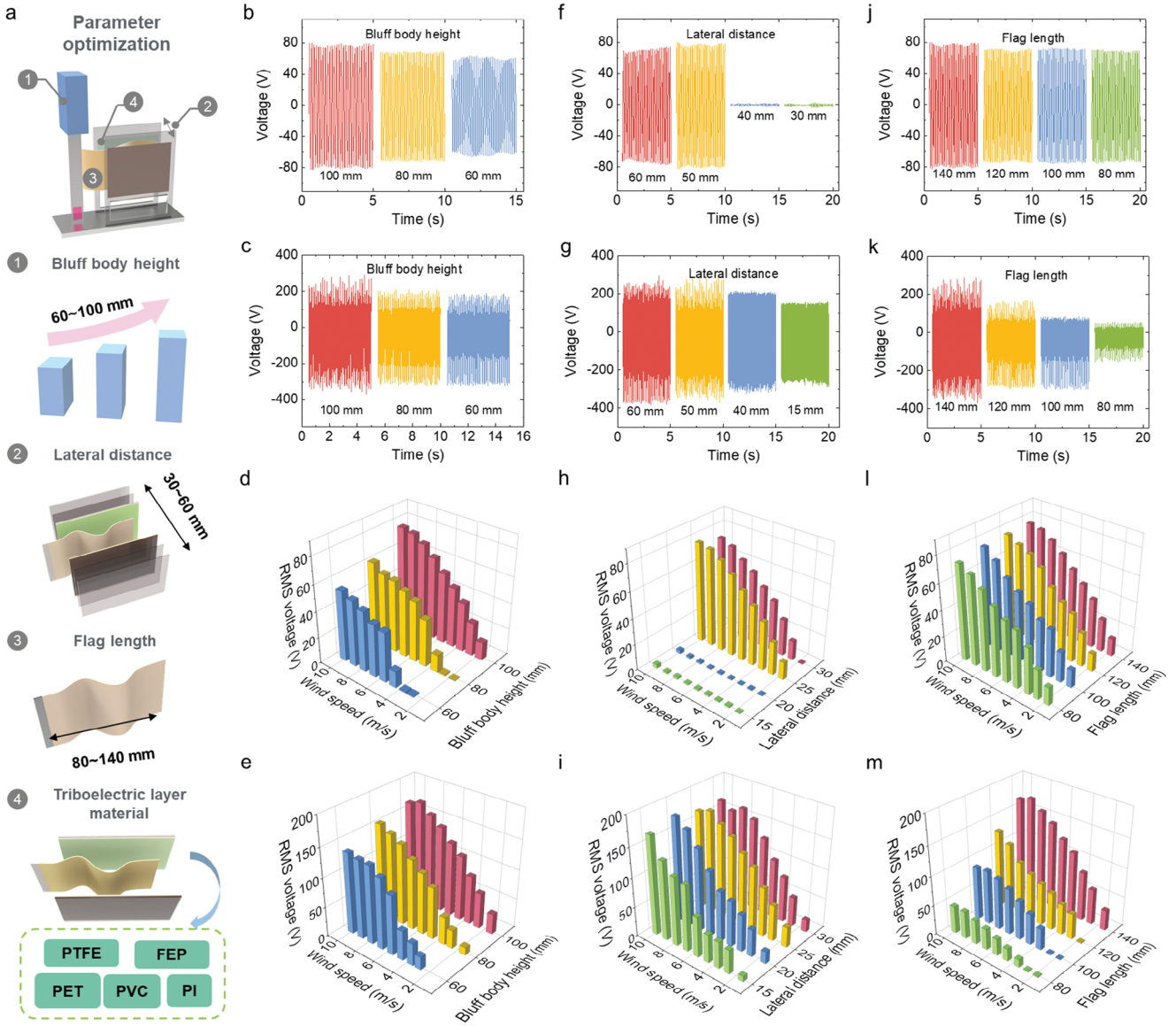

Figure 5. Parameter optimization of GFNG: a) optimized parameter and material; b) open-circuit voltage of GPEH and c) FTENG versus bluff body height at 5.7 m s^{-1}; d) RMS voltage of GPEH and e) FTENG versus bluff body height and wind speed; f) open-circuit voltage of GPEH and g) FTENG versus lateral distance at 5.7 m s^{-1}; h) RMS voltage of GPEH and i) FTENG versus lateral distance and wind speed; j) open-circuit voltage of GPEH and k) FTENG versus flag length at 5.7 m s^{-1}; l) RMS voltage of GPEH and m) FTENG versus flag length and wind speed.

schemes, with the exception of achieving the best operational bandwidth. Thus, the 0.6 mm beam thickness is selected after comprehensive consideration, and other parameters will be further optimized through experiments to improve the overall performance of the GFNG.

2.4. Parameter Optimization of GFNG

In Section 2.3, the parameters of the GPEH are determined through theoretical calculations to achieve optimal performance. In this section, parameter optimization is conducted under the integration of GPEH and FTENG through experimental tests to maximize the overall energy harvesting performance of the GFNG (see **Figure** 5a).

Although the bluff body height is theoretically determined in Section 2.3, its impact on the galloping displacement is more significant than the electrical output (see Figure S9, Supporting Information). This may affect the contact behavior of the FTENG and the overall performance of the GFNG. Thus, the bluff body height is varied from 60 to 100 mm in experimental tests and its effects are further investigated. According to Equation (8), the galloping force increases positively with bluff body height, leading to higher electrical output for piezoelectric energy harvesting at the same wind speed of 5.7 m s^{-1} (see Figure 5b). As a result, the contact behavior and voltage output of the FTENG are improved under more pronounced galloping conditions (see Figure 5c). Figure 5d and Figure S11a (Supporting Information) demonstrate that the optimal performance is achieved with a bluff body

height of 100 mm across wind speeds from 1.7 to 10 m s^{-1}. Meanwhile, the cut-in wind speed of the GPEH declines from 5.5 to 1.7 m s^{-1}. This reduction is crucial for optimizing GFNG, as it enhances the RMS and peak-to-peak voltages of the FTENG at lower wind speeds (see Figure 5e; Figure S11b, Supporting Information).

Furthermore, the lateral distance between the two baffles is increased from 30 to 60 mm. This adjustment not only affects the fluttering behavior of the conductive flag, but also the physical boundary of the GPEH. The voltage signals of the GPEH and FTENG at 5.7 m s^{-1} are selected for an intuitive comparison, as shown in Figure 5f,g. The GPEH is not activated with distances of 30 and 40 mm, likely due to the small distance impacting the flow field and preventing the onset of galloping. The GPEH achieves the best voltage performance with a lateral distance of 50 mm, while the FTENG yields maximum voltage at 60 mm. The performance of the GPEH and FTENG at different wind speeds is further investigated in Figure 5h,i. The electrical output of the GPEH with a 50 mm lateral distance (see Figure 5h; Figure S12a, Supporting Information) is optimal across 1.7-10 m s^{-1}. For the FTENG, when the distances are 50 and 60 mm, the RMS and peak-to-peak voltages (see Figure 5i; Figure S12b, Supporting Information) are relatively high because of the galloping activation. Notably, at low wind speeds below 5.7 m s^{-1}, a distance of 50 mm showcases better energy harvesting capacity. With the current GPEH configuration, the beam displacement at different wind speeds is calculated based on the aerodynamic model, as depicted in Figure S13 (Supporting Information), and the displacements of the top, bottom, and center of the flag induced by galloping are summarized in Figure S14 (Supporting Information). At wind speeds of 3–6 m s^{-1}, the displacement from the flag center (20–30 mm) closely matches the distance from the baffles to the GPEH center (25 mm). This suggests that the flag's displacement induced by galloping significantly enhances the contact behavior between the textile and the PTFE, markedly improving the performance of triboelectric energy harvesting (see Figure S3e, Supporting Information).

Subsequently, the flag length is varied from 100 to 140 mm. As shown in Figure 5j, the impact of different flag lengths on the GPEH is minimal, with minor differences potentially caused by slight variations in fluttering frequency and intensity. However, a longer flag significantly increases the output voltage of the FTENG due to an increased contact area (see Figure 5k). Taking the wind speed as a variable, the impacts of the flag length on the GPEH's RMS and peak-to-peak performance are shown to be negligible in Figure 5l and Figure S15a (Supporting Information). On the other hand, a longer flag facilitates a higher RMS and peak-to-peak voltage output of the FTENG (see Figure 5m; Figure S15b, Supporting Information) across the operational wind speed range. Meanwhile, the flutter critical wind speed declines from 3.6 to 1.4 m s^{-1}, indicating an enhanced capacity for breeze energy harvesting.

Finally, to improve the performance of the FTENG from a material perspective, various triboelectric layer materials on the baffles are considered, as shown in Figure S16 (Supporting Information). The results presented are facilitated by both the material's electron affinity and compliance. Generally, a higher electron affinity enhances the electrical output of the FTENG, while greater compliance improves the fluttering contact behavior, further boosting the FTENG's electrical performance. The PTFE membrane exhibits the best performance due to its advantages in both aspects.

2.5. Energy Harvesting Capacity Optimization

The average power of the GPEH and FTENG is investigated by tuning external resistance, as illustrated in **Figure 6**a,b. The optimal average power of the GPEH increases from 0.4 to 4.6 mW with an increased wind speed ranging from 3 to 10 m s^{-1}. Meanwhile, the optimal resistance value declines from 800 to 500 kΩ. Similarly, the optimal average performance of the FTENG increases from 0.16 to 1.6 mW with an increased wind speed ranging from 3 to 10 m s^{-1}, along with the optimal resistance value shifting from 7.4 to 2.9 MΩ. Compared with a pure FTENG, the optimal resistance for average power (see Figure S17a, Supporting Information) remains relatively unchanged. Figure 6c evaluates the optimal average power of the GFNG. Thanks to the advantages of the flexible textile, the FTENG in the GFNG can be activated at 1.4 m s^{-1}, generating an average power of 70 μW. As wind speed increases, leading to more intense flutter and galloping responses, the GFNG achieves a considerable average power of 6.3 mW at 10 m s^{-1}. In Figure S18 (Supporting Information), the average power of the GFNG is compared with previous hybrid nanogenerators, highlighting its superiority in sustained power generation. Figure 6d,e focus on the peak power of the GPEH and FTENG as a function of external resistance. The GPEH attains a peak power ranging from 0.86 to 11.5 mW as wind speed increases from 3 to 10 m s^{-1}, while the FTENG achieves a peak power range of 6–57 mW (power density range of 0.8–7.1 W m^{-2}) with the optimal resistance decreasing from 3.8 to 2 MΩ. This makes the FTENG particularly suitable for applications requiring high instantaneous power. Although the average power improvement brought by the GFM is diluted at high wind speeds, the improvement in peak power is persistently significant compared to that of a pure FTENG (see Figure S17b, Supporting Information). In addition, the enhanced FTENG exhibits a relatively high peak power with a 500 kΩ resistance at 6 and 10 m s^{-1}, facilitating easier generation of high instantaneous power. Figure 6f compares the remarkable peak power density of the enhanced FTENG with other wind-driven TENGs,[42,43,60–64] further demonstrating the superiority of our design.

Capacitor charging tests are conducted to evaluate the power supply capability for electronic devices, as shown in Figure 6g–i. Although the FTENG is better at providing instantaneous high power, it can also charge capacitors separately to power electronic devices. A 47 μF capacitor can be charged to 3.6 V in 30 s by the FTENG at 3 m s^{-1}, as depicted in Figure 6g. The charging speed of FTENG is slower compared to that of GPEH, due to its higher internal resistance, which can be improved through effective interface circuit design. Additionally, the collaborative operation of the GPEH and FTENG can further improve the charging speed. As illustrated in Figure 6h, the capacitor charging speeds up at higher wind speeds. It only takes 1.7 s to charge the 47 μF capacitor to 5 V at 10 m s^{-1}. Moreover, in Figure 6i, the capacitor capacity is continuously increased, and a 470 μF capacitor can be charged to 3.1 V within 12 s, showcasing the GFNG's ability to power conventional electronics.

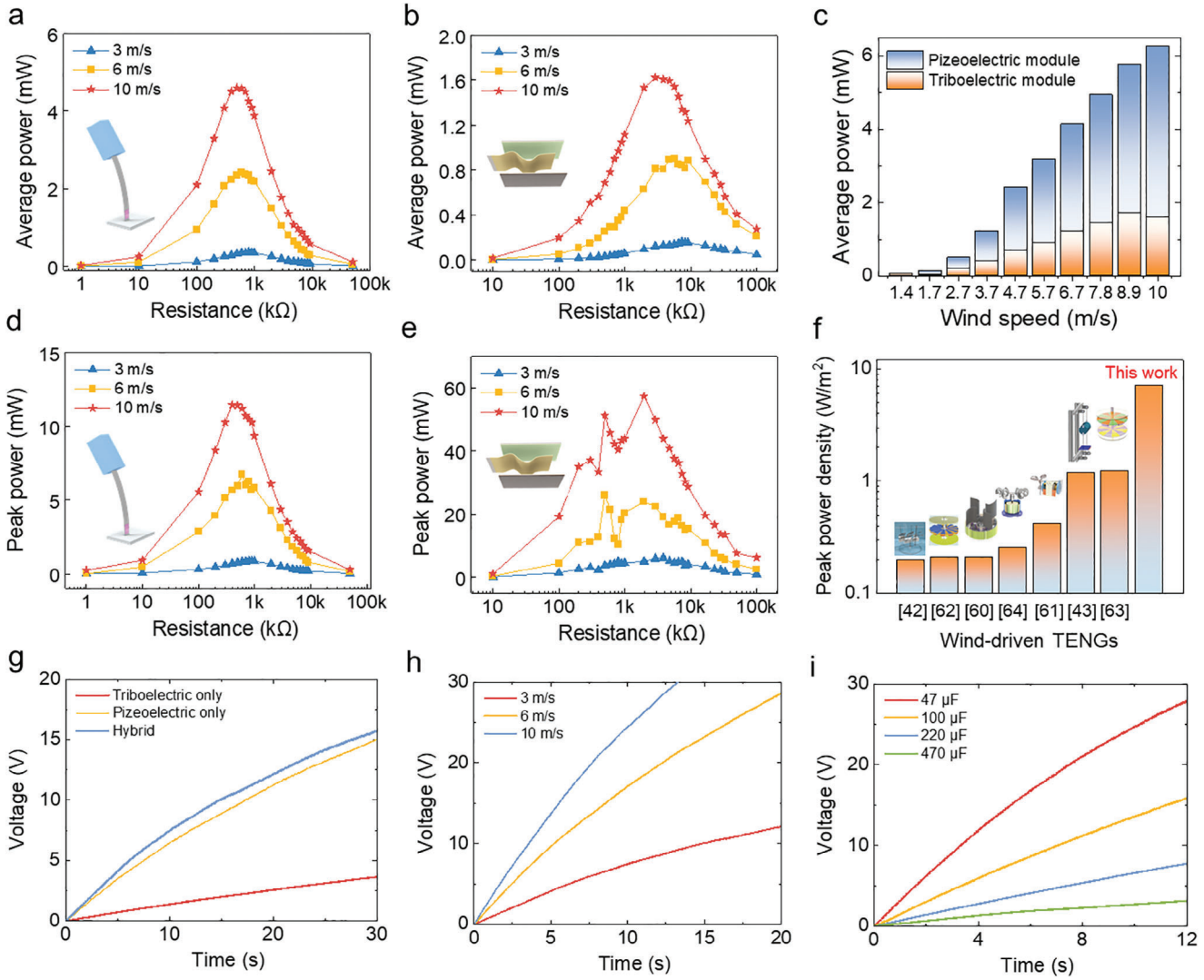

Figure 6. Energy harvesting performance optimization and capacitor charging tests: a) average power of GPEH versus external resistance; b) average power of FTENG with GFM versus external resistance; c) optimal average power of GFNG at different wind speeds; d) peak power of GPEH versus external resistance; e) peak power of FTENG with GFM versus external resistance; f) comparison of the peak power density of FTENG with GFM with other wind-driven TENGs; g) charging a 47 μF capacitor at 3 m s^{-1} with FTENG, GPEH and hybrid configurations; h) charging a 47 μF capacitor with GFNG at different wind speeds; i) charging performance of GFNG with different capacitors at 10 m s^{-1}.

2.6. Application Demonstrations

In this section, the GFNG is employed to power some conventional electronics to demonstrate its superiority in structural design and energy harvesting performance. Due to its remarkable peak power, the FTENG in the GFNG successfully lights 508 LEDs at 6 m s^{-1}, as illustrated in **Figure** 7a. A visual demonstration video is also supplemented in Movie S1 (Supporting Information). Figure 7b illustrates the experimental setup for the demonstration of the GFNG powering a WSN. The WSN implements the real time monitoring of environmental temperature, with the acquired signals transmitted wirelessly and displayed on mobile terminals. As shown in Figure 7c, the WSN integrates a rectifier unit (RU), energy management unit (EMU), and signal transmission unit (STU). The AC voltage outputs generated by the FTENG and GPEH are converted into DC voltage for the EMU by two full-bridge rectifiers. The EMU incorporating a buck converter (BC), storage capacitor, and hysteresis comparator, is implemented based on an LTC3588-1 chip, with a complementary design to lower the energy consumption of the circuit and WSN. The hysteresis comparator outputs the normal operation instruction P_{good} or sleep instruction P_{sleep} based on the energy level in the capacitor. During normal operation with instruction P_{good}, P_s sets and the BC operates when the capacitor voltage is greater than 5 V, while P_c sets and the BC turns off when the capacitor voltage drops below 3.4 V. When sleep instruction P_{sleep} is active, the STU saves the critical data and enters ultra-low power sleep mode. A detailed view of the WSN prototype is illustrated in Figure 7d. Figure 7e illustrates the circuit voltage when powered by the GFNG at different wind speeds. The circuit is first charged to 5 V, after which the voltage decreases, indicating that the WSN is activated and energy is transferred to the STU. As wind speed

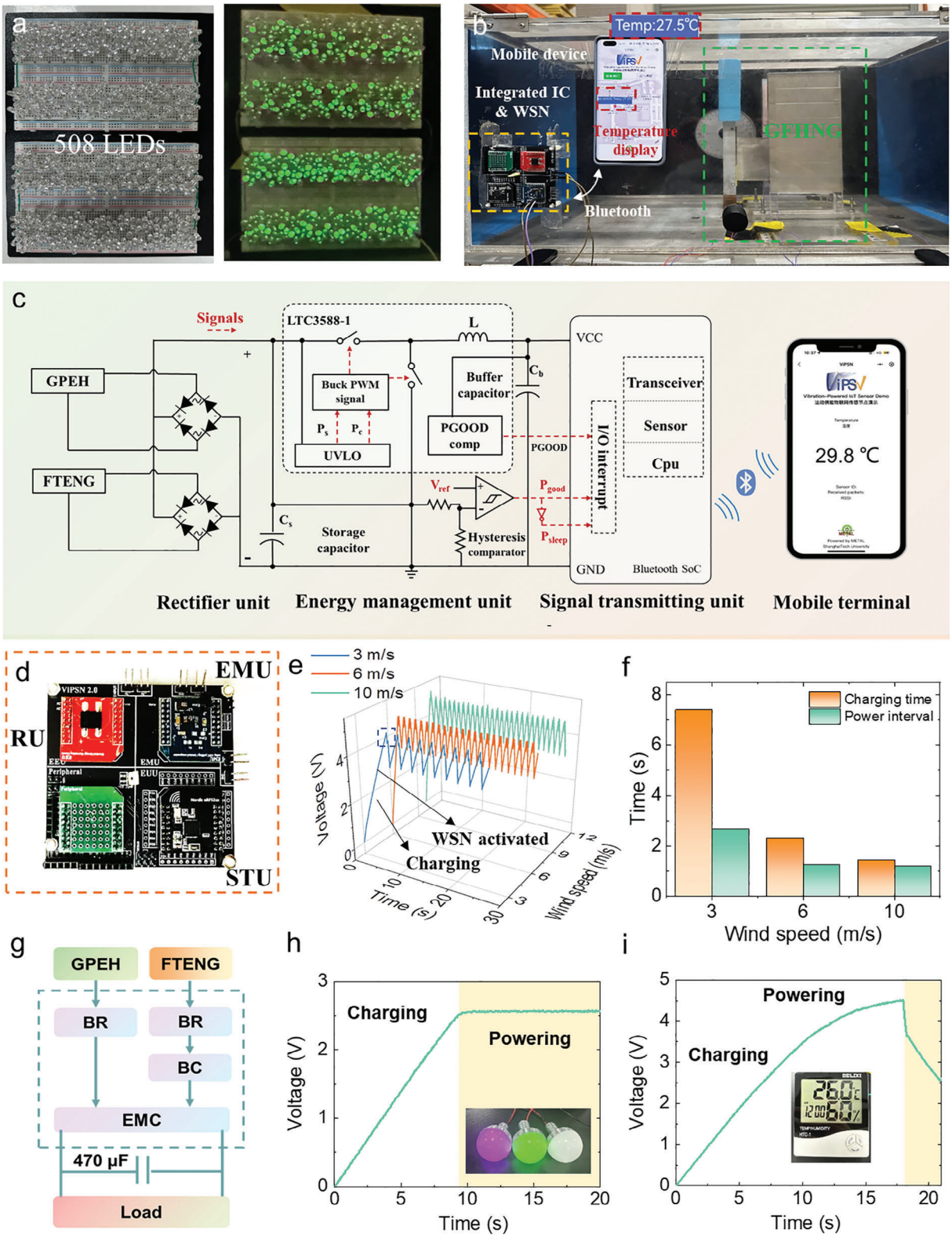

Figure 7. Application demonstrations for GFNG: a) lighting 508 LEDs with FTENG; b) photograph of GFNG powering an integrated WSN; c) principle and d) photograph of the integrated WSN; e) instantaneous voltage of WSN powered by GFNG; f) charging time and power interval of WSN powered by GFNG at different wind speeds; g) circuit configuration for some common electronics application; h) lighting bulbs; i) powering a humidity sensing system.

increases, the WSN is activated more frequently within the same time frame. Figure 7f summarizes the charging time and power interval of the WSN. At a low wind speed of 3 m s^{-1}, the WSN operates well with a 7.4 s charging and realizes a 2.7 s signal transmission interval. Correspondingly, a demonstration video is provided in Movie S2 (Supporting Information). At 10 m s^{-1}, the charging time and signal transmission interval are shortened to 1.4 s and 1.2 s, respectively, indicating that the WSN can be activated almost instantly. A circuit configuration, as shown in Figure 7g, is employed to demonstrate the application for other electronics. The GFNG lights three bulbs after a 9 s pre-charging period, with the supply voltage remaining almost constant (see Figure 7h). Additionally, it successfully powers a humidity and temperature sensing system, highlighting the enormous potential in daily applications (see Figure 7i).

3. Conclusion

In summary, we have developed a highly efficient, aerodynamics-driven hybrid GFNG that utilizes two types of FIVs, galloping and flutter, to enhance breeze energy harvesting. The GFNG integrates a GPEH and an FTENG leveraging a carefully designed GFM. The GFM triggers galloping-induced beam oscillations at low wind speeds, intensifying flag flutter and boosting triboelectric energy harvesting up to six times. Through parameter optimization, beam thickness is meticulously determined to be 0.6 mm based on theoretical analysis results. Additionally, a bluff body height of 100 mm is selected to guarantee a low cut-in wind speed of the GPEH and sufficient galloping displacements for fluttering contact behavior improvement under breeze scenarios. An optimal distance of 50 mm is determined, as small distances of 30 and 40 mm disrupt the flow field, hindering the operation of the GPEH. The GFNG exhibits an optimal average power range of 70 μW–6.3 mW across a broad operational wind speed bandwidth of 1.4–10 m s^{-1}. Meanwhile, a remarkable power density of 7.1 W m^{-2} is realized by the enhanced FTENG at 10 m s^{-1}. Notably, peak power outputs of the FTENG are observed with a 500 kΩ resistance at both 6 and 10 m s^{-1}, facilitating the easier implementation of high instantaneous power applications. Finally, the GFNG successfully powers 508 LEDs, a temperature monitoring WSN, lamp bulbs, and a hygrometer. At a low wind speed of 3 m s^{-1}, the WSN is activated after 7.4 s of charging, achieving continuous temperature data transmission every 2.7 s. This comprehensive design, combining galloping and flutter effects with precise parameter optimization, marks a significant advancement in the field of aerodynamics-driven nanogenerators, and holds substantial promise for remote environmental monitoring and urban infrastructure applications.

4. Methods

Simulations of GFNG: The electrical potential of the FTENG was simulated using COMSOL Multiphysics 5.6 via the Electrostatic Module. The modal analysis for the GPEH was implemented using ANSYS 19.0. The 3D model of the GPEH was developed in SOLIDWORKS 2020, and then imported into ANSYS 19.0 for finite element simulations. The aero-electromechanical model of the GPEH was programmed in MATLAB R2019a, and the final state equations were solved using the ode45 solver.

Fabrication of GFNG: The GFNG comprises a GPEH and an FTENG. The GPEH incorporates a bluff body, a flexible beam, and a MFC. The rectangle bluff body, made of foam, has a characteristic length, width, and height of 50 × 30 × 100 mm^3. The length, width, and thickness of the aluminum beam is 235 × 20 × 0.6 mm^3. The MFC (M2814-P2), with dimensions of 28 × 14 × 0.3 mm^3, was attached to the fixed end of the beam using epoxy resin adhesive. The FTENG consisted of a flag, electrodes, triboelectric layers, and baffles. The flag was made of Nickel-coated conductive textile with a length, thickness, and height of 140 × 0.1 × 80 mm^3. The copper electrodes attached to the inside of acrylic baffles possess a length, thickness, and height of 100 × 0.1 × 100 mm^3. The triboelectric layers, made of PEFE membranes, were attached to the copper electrodes with the same geometric dimensions.

Electrical Measurement of GFNG: The electrical characteristics of the GFNG were characterized through wind tunnel tests in the CEE Protective Engineering Lab of Nanyang Technological University. A wind tunnel (FM670 from EdLabQUIP) with a cross section of 300 × 300 mm^2 was employed, enabling a maximum wind speed of 15 m s^{-1}. A four-channel oscilloscope (Tektronix MSO44) and data acquisition unit (Kistler LabAmp 5165A) were used to acquire the electrical signals of the GFNG. For resistance optimization and capacitor charging tests, a resistance substitute (IET RS-200 W) and a capacitance substitute (IET RCS-500) were employed.

Circuit Hardware Implementation: The printed circuit board of integrated WSN for mobile temperature monitoring was implemented using Altium Designer 20, and the software and algorithm-related works were developed using Keil uVision5. The EMC was designed with a DC-DC converter controller chip LT3588-1 for voltage regulation with an energy conversion efficiency of 80–90%. A low-power consumption voltage comparator MIC841 with adjustable hysteresis was used to control the circuit's operating mode. Signal transmission between the WSN and mobile phones was realized by Bluetooth technology. The STU was designed with a Bluetooth system on chip nRF52832. Mobile phones received signals by running customized software on WeChat.

Supporting Information

Supporting Information is available from the Wiley Online Library or from the author.

Acknowledgements

This research is sponsored by the National Natural Science Foundation of China (Grant No. 52305135), the National Natural Science Foundation of China (Grant No. 12202276), the Guangzhou Municipal Science and Technology Project (Grant No. 2023A03J0011), Guangdong Provincial Key Lab of Integrated Communication, Sensing and Computation for Ubiquitous Internet of Things (No. 2023B1212010007), NTU grant 020671-00001, the China Scholarship Council (Grant No. 202206260157), and innovative research team of high-level local universities in Shanghai.

Conflict of Interest

The authors declare no conflict of interest.

Data Availability Statement

The data that support the findings of this study are available from the corresponding author upon reasonable request.

Keywords

flow-induced vibration, piezoelectric, triboelectric, wind energy harvesting, wireless sensor node

Received: August 7, 2024
Revised: November 2, 2024
Published online: November 22, 2024

[1] L.-C. Zhao, H.-X. Zou, K.-X. Wei, S.-X. Zhou, G. Meng, W.-M. Zhang, *Adv. Energy Mater.* **2023**, *13*, 2300557.
[2] H. Fu, X. Mei, D. Yurchenko, S. Zhou, S. Theodossiades, K. Nakano, E. M. Yeatman, *Joule* **2021**, *5*, 1074.
[3] J. Zuo, L. Dong, F. Yang, Z. Guo, T. Wang, L. Zuo, *Renew. Energy* **2023**, *202*, 56.
[4] L. Dong, Y. Ke, Y. Liao, J. Wang, M. Gao, Y. Yang, J. Li, F. Yang, *Adv. Funct. Mater.* **2024**, 2410566.
[5] Q. Wen, X. He, Z. Lu, R. Streiter, T. Otto, *Nano Mater. Sci.* **2021**, *3*, 170.
[6] H.-X. Zou, L.-C. Zhao, Q.-H. Gao, L. Zuo, F.-R. Liu, T. Tan, K.-X. Wei, W.-M. Zhang, *Appl. Energy* **2019**, *255*, 113871.
[7] Z. Ren, L. Wu, Y. Pang, W. Zhang, R. Yang, *Nano Energy* **2022**, *100*, 107522.
[8] F.-R. Fan, Z.-Q. Tian, Z. L. Wang, *Nano Energy* **2012**, *1*, 328.
[9] G. Zhu, J. Chen, T. Zhang, Q. Jing, Z. L. Wang, *Nat. Commun.* **2014**, *5*, 3426.
[10] Y. Zi, H. Guo, Z. Wen, M.-H. Yeh, C. Hu, Z. L. Wang, *ACS Nano* **2016**, *10*, 4797.
[11] K. Zhao, W. Sun, X. Zhang, J. Meng, M. Zhong, L. Qiang, M.-J. Liu, B.-N. Gu, C.-C. Chung, M. Liu, F. Yu, Y.-L. Chueh, *Nano Energy* **2022**, *91*, 106649.
[12] C. Wu, T. W. Kim, J. H. Park, H. An, J. Shao, X. Chen, Z. L. Wang, *ACS Nano* **2017**, *11*, 8356.
[13] S. Liu, W. Qing, D. Zhang, C. Gan, J. Zhang, S. Liao, K. Wei, H. Zou, *Nano Energy* **2024**, *128*, 109849.
[14] Y.-G. Heo, C.-L. Kim, G.-M. Kim, K. Lee, W. Hwang, J.-W. Lee, *Surf. Interfaces* **2021**, *27*, 101525.
[15] B. Zhang, Q. Gao, W. Li, M. Zhu, H. Li, T. Cheng, Z. L. Wang, *Adv. Funct. Mater.* **2023**, *33*, 2304839.
[16] Q. Bai, C.-Z. Gan, T. Zhou, Z.-C. Du, J.-H. Wang, Q. Wang, K.-X. Wei, H.-X. Zou, *Energy Convers. Manage.* **2024**, *306*, 118323.
[17] F. Xi, Y. Pang, W. Li, T. Jiang, L. Zhang, T. Guo, G. Liu, C. Zhang, Z. L. Wang, *Nano Energy* **2017**, *37*, 168.
[18] X. Yu, S. Fu, X. Zuo, J. Zeng, C. Shan, W. He, W. Li, C. Hu, *Adv. Funct. Mater.* **2022**, *32*, 2207498.
[19] Z. Wu, Z. Cao, R. Ding, S. Wang, Y. Chu, X. Ye, *Nano Energy* **2021**, *89*, 106425.
[20] K.-J. I. Egbe, A. Matin Nazar, P. Jiao, *Int. J. Mech. Sci.* **2022**, *235*, 107722.
[21] C. Ye, K. Dong, J. An, J. Yi, X. Peng, C. Ning, Z. L. Wang, *ACS Energy Lett.* **2021**, *6*, 1443.
[22] Y. Luo, P. Chen, L. N. Y. Cao, Z. Xu, Y. Wu, G. He, T. Jiang, Z. L. Wang, *Adv. Funct. Mater.* **2022**, *32*, 2205710.
[23] P. Wang, L. Pan, J. Wang, M. Xu, G. Dai, H. Zou, K. Dong, Z. L. Wang, *ACS Nano* **2018**, *12*, 9433.
[24] L. Dong, J. Zuo, *Mech. Syst. Signal Process.* **2025**, *223*, 111940.
[25] L. Dong, G. Hu, J. Yu, C. Zhao, S. Qu, Y. Yang, *Appl. Energy* **2023**, *347*, 121388.
[26] F. Zheng, Y. Zhou, S. Hu, R. Li, Z. L. Wang, Z. Wu, *Adv. Energy Mater.* **2022**, *12*, 2201966.
[27] M. Zhu, Y. Yu, J. Zhu, J. Zhang, Q. Gao, H. Li, Y. Zhang, Z. L. Wang, T. Cheng, *Adv. Energy Mater.* **2023**, *13*, 2303119.
[28] J. Wang, L. Geng, L. Ding, H. Zhu, D. Yurchenko, *Appl. Energy* **2020**, *267*, 114902.
[29] X. Ma, S. Zhou, *Energy Convers. Manage.* **2022**, *254*, 115223.
[30] Y. Yang, L. Zhao, L. Tang, *Appl. Phys. Lett.* **2013**, *102*, 064105.
[31] Z. Lai, S. Wang, L. Zhu, G. Zhang, J. Wang, K. Yang, D. Yurchenko, *Mech. Syst. Signal Process.* **2021**, *150*, 107212.
[32] H. Tian, X. Shan, X. Li, J. Wang, *Appl. Energy* **2023**, *340*, 120979.
[33] S. Chen, L. Zhao, *Appl. Energy* **2023**, *331*, 120423.
[34] L. Zhao, Y. Yang, *Appl. Energy* **2018**, *212*, 233.
[35] J. Wang, S. Sun, G. Hu, Y. Yang, L. Tang, P. Li, G. Zhang, *Energy Convers. Manage.* **2021**, *243*, 114414.
[36] J. Xing, M. Rezaei, H. Dai, W.-H. Liao, *Appl. Phys. Lett.* **2023**, *122*, 153902.
[37] Y. Hu, B. Yang, X. Chen, X. Wang, J. Liu, *Energy Convers. Manage.* **2018**, *162*, 145.
[38] B. Tang, X. Fan, J. Wang, W. Tan, *Int. J. Mech. Sci.* **2022**, *236*, 107749.
[39] J. Liu, B. Bao, J. Chen, Y. Wu, Q. Wang, *Mech. Syst. Signal Process.* **2023**, *185*, 109814.
[40] J. Wang, B. Xia, D. Yurchenko, H. Tian, *Mech. Syst. Signal Process.* **2023**, *205*, 110838.
[41] J. Wang, S. Zhou, Z. Zhang, D. Yurchenko, *Energy Convers. Manage.* **2019**, *181*, 645.
[42] H. Li, J. Wen, Z. Ou, E. Su, F. Xing, Y. Yang, Y. Sun, Z. L. Wang, B. Chen, *Adv. Funct. Mater.* **2023**, *33*, 2212207.
[43] L. Zhang, B. Meng, Y. Tian, X. Meng, X. Lin, Y. He, C. Xing, H. Dai, L. Wang, *Nano Energy* **2022**, *95*, 107029.
[44] C. Zhao, G. Hu, Y. Yang, *Mech. Syst. Signal Process.* **2022**, *177*, 109185.
[45] L. Zhang, B. Meng, Y. Xia, Z. Deng, H. Dai, P. Hagedorn, Z. Peng, L. Wang, *Nano Energy* **2020**, *70*, 104477.
[46] S. Yuan, Q. Zeng, D. Tan, Y. Luo, X. Zhang, H. Guo, X. Wang, Z. L. Wang, *Nano Energy* **2022**, *100*, 107465.
[47] Z. Li, S. Zhou, Z. Yang, *Int. J. Mech. Syst. Dyn.* **2022**, *2*, 82.
[48] Z. Zhao, X. Pu, C. Du, L. Li, C. Jiang, W. Hu, Z. L. Wang, *ACS Nano* **2016**, *10*, 1780.
[49] Y. Wang, E. Yang, T. Chen, J. Wang, Z. Hu, J. Mi, X. Pan, M. Xu, *Nano Energy* **2020**, *78*, 105279.
[50] Y. Wang, X. Liu, T. Chen, H. Wang, C. Zhu, H. Yu, L. Song, X. Pan, J. Mi, C. Lee, M. Xu, *Nano Energy* **2021**, *90*, 106503.
[51] W. Sun, Z. Ding, Z. Qin, F. Chu, Q. Han, *Nano Energy* **2020**, *70*, 104526.
[52] J. Bae, J. Lee, S. Kim, J. Ha, B.-S. Lee, Y. Park, C. Choong, J.-B. Kim, Z. L. Wang, H.-Y. Kim, J.-J. Park, U. I. Chung, *Nat. Commun.* **2014**, *5*, 4929.
[53] L. Dong, Q. Tang, C. Zhao, G. Hu, S. Qu, Z. Liu, Y. Yang, *Nano Energy* **2024**, *119*, 109057.
[54] L. Dong, G. Hu, Y. Zhang, W. Ding, S. Qu, Q. Tang, C. Zhao, Y. Yang, F. Yang, *Nano Energy* **2024**, *124*, 109508.
[55] Y. Zhang, S.-C. Fu, K. C. Chan, D.-M. Shin, C. Y. H. Chao, *Nano Energy* **2021**, *88*, 106284.
[56] L. Qin, L. Zhang, J. Feng, F. Zhang, Q. Han, Z. Qin, F. Chu, *Nano Energy* **2024**, *124*, 109506.
[57] Z. Zheng, H. Yin, B. Wang, Y. Chen, H. Liu, Y. Guo, *Nano Energy* **2023**, *108*, 108236.
[58] M. F. Daqaq, A. H. Alhadidi, S. Khazaaleh, *Nonlinear Dyn.* **2022**, *110*, 3001.
[59] A. Barrero-Gil, G. Alonso, A. Sanz-Andres, *J. Sound Vib.* **2010**, *329*, 2873.
[60] H.-X. Zou, L.-C. Zhao, Q. Wang, Q.-H. Gao, G. Yan, K.-X. Wei, W.-M. Zhang, *Nano Energy* **2022**, *95*, 106990.
[61] S. Liu, X. Li, Y. Wang, Y. Yang, L. Meng, T. Cheng, Z. L. Wang, *Nano Energy* **2021**, *83*, 105851.
[62] C. Zhang, Y. Liu, B. Zhang, O. Yang, W. Yuan, L. He, X. Wei, J. Wang, Z. L. Wang, *ACS Energy Lett.* **2021**, *6*, 1490.
[63] L. Long, W. Liu, Z. Wang, W. He, G. Li, Q. Tang, H. Guo, X. Pu, Y. Liu, C. Hu, *Nat. Commun.* **2021**, *12*, 4689.
[64] X. Li, Y. Cao, X. Yu, Y. Xu, Y. Yang, S. Liu, T. Cheng, Z. L. Wang, *Appl. Energy* **2022**, *306*, 117977.